J Adv Ceram

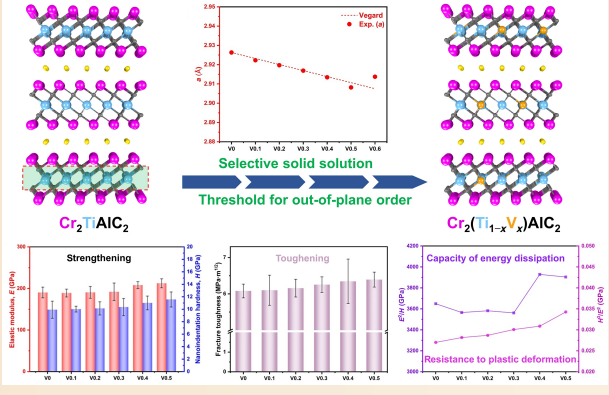
Research Article

Out-of-plane order retention below the solubility threshold in V-strengthened Cr_2TiAlC_2 and its mechanical benefits

Cheng-Feng Du, Linze Fan, Xuan Luo, Yaqing Xue, Shiyao Lei, Yifei Xiao, Wenbo Wu, Weihong Qi, Hong Yu✉

Cite this article: Du C-F, Fan L, Luo X, et al. *J Adv Ceram* 2026, **15**(8): 9221336. https://doi.org/10.26599/JAC.2026.9221336

ABSTRACT: The development of MAX materials with out-of-plane chemically ordered structures (o-MAX) represents a key frontier in advanced structural ceramics. However, their synthesis is challenging due to elemental combination constraints and molar ratio limitations. This study successfully synthesized a series of novel $Cr_2(Ti_{1-x}V_x)AlC_2$ (x = 0–0.6) quinary o-MAX materials by rationally selecting element combinations and regulating their proportions. Analysis via X-ray diffraction (XRD) Rietveld refinement and aberration-corrected transmission electron microscopy revealed that the solid solution threshold for V-induced suppression of out-of-plane chemical ordering is x = 0.5. When $x \le 0.5$, V selectively forms solid solutions with Ti at the 2*a* Wyckoff site, preserving out-of-plane chemical order. However, when the V proportion exceeds the solid solution limit ($x > 0.5$), the structure undergoes an ordered–disordered transition, accompanied by the migration of V and Ti to the 4*f* Wyckoff site. Furthermore, the out-of-plane chemically ordered introduction of V achieves comprehensive enhancement of mechanical properties. The optimal composition $Cr_2(Ti_{0.5}V_{0.5})AlC_2$ sample exhibits significant improvements in both hardness and toughness. Based on the nanoindentation hardness (H) and elastic modulus (E), the materials' capacity for energy dissipation (E^2/H) and resistance to plastic deformation (H^3/E^2) are analyzed. Accordingly, its E^2/H and H^3/E^2 ratios increase by approximately 7% and 27%, respectively, highlighting the synergistic strengthening–toughening effect. This work not only expands the variety of o-MAX phases but also establishes a clear microstructure–property relationship, demonstrating that a selective site solid solution is an effective strategy for designing high-performance MAX phase ceramics.



KEYWORDS: MAX phase ceramics; chemical ordering; mechanical property; solid solution

1 Introduction

MAX phase ceramics, also known as ternary layered carbides/nitrides, have garnered significant attention in recent years due to their unique nanolayer structure [1–6]. Their crystal structure can be described as alternating stacks of $M_{n+1}X_n$ (n = 1–4) layers with a rock salt structure and densely packed A-atom (main-group element) planes along the *c*-direction [7–11]. The unique crystal structure integrates both extremely strong covalent or ionic M–X interactions and weak M–A metallic bonds, which confer the MAX phase with outstanding toughness and ductility, combining the advantages of both metals and ceramics [12–17]. Recently, an out-of-plane arrangement involving two transition metals (M) occupying distinct Wyckoff sites within a single $M_{n+1}C_n$ layer of the 312 (M_3AlC_2) and 413 (M_4AlC_3) phases has been discovered within the MAX phase family, i.e., MAX materials with out-of-plane chemically ordered structures (o-MAX), which has quickly attracted particular attention [11,18–20]. Cr_2TiAlC_2, in which Cr and Ti occupy the 4*f* and 2*a* Wyckoff sites, respectively, exemplifies this phenomenon [21,22]. The out-of-plane arrangement of these two transition metals introduces not only a versatile composition but also inhomogeneous M–C bonds within the carbide skeleton of Cr_2TiAlC_2 and thus yields a set of properties markedly improved over those of Ti_3AlC_2, comprising high toughness, high strength, and greater oxidation resistance [23,24]. For this reason, the design of o-MAX with desired elemental compositions offers a promising pathway toward developing high-performance materials within the MAX phase family. However, the formation of out-of-plane chemically ordered structures is particularly challenging, as it requires meeting several strict criteria: 4*f* atoms that do not readily form binary rock-salt type carbides, a

State Key Laboratory of Solidification Processing, Center of Advanced Lubrication and Seal Materials, Northwestern Polytechnical University, Xi'an 710072, China.

✉ Corresponding author. E-mail: yh@nwpu.edu.cn

Received: March 30, 2026; Revised: June 16, 2026; Accepted: June 18, 2026

© The Author(s) 2026. This is an open access article under the terms of the Creative Commons Attribution 4.0 International License (CC BY 4.0, http://creativecommons.org/licenses/by/4.0/).

sufficiently large electronegativity difference between the 4*f* atom and Al, and a minimal size mismatch between the 4*f* and 2*a* atoms [18,25].

Elemental solid solution in the M, A, or X sites of MAX materials is a common approach for regulating the material's mechanical, tribological, and oxidation resistance properties [7,26]. Significant progress has been made in this area, particularly in coating applications, where controlled elemental substitution can lead to substantial improvements in material performance [27,28]. However, extending such solid solution strategies to o-MAX phases presents additional challenges, as the maintenance of long-range chemical order imposes stricter constraints on elemental composition and atomic size matching [20,29]. On this account, alternative attempts through solid solution have been made to tailor the elemental composition of o-MAX phases over the past several years, yet most have still ended in failure. For instance, Mo is introduced as a solid solution element into Cr_2TiAlC_2, motivated by its tendency to order with Ti in Mo_2TiAlC_2. However, in the resulting compounds, the intended chemical ordering is partially disrupted [30]. The collapse of atomic ordering is initially believed to arise from a violation of the rigid stoichiometry governing atomic occupancy at specific Wyckoff sites [31]. In contrast, recent studies have attributed this destabilization to the rising configurational entropy stemming from the growing complexity of both elemental composition and atomic ratios [29,32,33]. This conflict is particularly evident in the MAX phase system involving Cr, Ti, and V [34–37]. As observed in $(Cr_{0.5}V_{0.5})_3AlC_2$, V is found to occupy both the 4*f* and 2*a* sites, whereas Cr exclusively resides at the 4*f* site [37]. This selective occupancy is attributed to the intrinsic stoichiometric constraints governing site preference. However, when half of the Cr atoms in Cr_2TiAlC_2 are replaced by an equimolar amount of V, the resulting $(CrTiV)_3AlC_2$ exhibits a different elemental distribution: The 4*f* site is now occupied by a solid solution of Cr, Ti, and V, while the 2*a* site contains only Ti and V [38]. The migration of Ti into the 4*f* site signifies a notable increase in configurational entropy. These observations suggest that as the compositional complexity increases, the rigid stoichiometric boundaries governing the transition from chemical ordering to disorder become blurred. Thus, elucidating the critical atomic ratio that dictates this order–disorder transition is essential to resolving the apparent contradiction.

In this work, V atoms are incorporated into Cr_2TiAlC_2 along a continuous compositional gradient, where they substitutionally replace Ti atoms on an equimolar basis, i.e., $Cr_2(Ti_{1-x}V_x)AlC_2$ (x = 0–0.6). Combining Rietveld refinement with atomic-resolution transmission electron microscopy (TEM) characterization, the V solubility threshold at which the Cr_2TiAlC_2 phase can maintain its out-of-plane chemical order was determined to be x = 0.5. When the V content exceeds this threshold, the material undergoes an order–disorder transition. Moreover, nanoindentation and Vickers hardness (H_v) testing are performed on this series of samples as well. Fracture toughness (K_{IC}) is evaluated using the energy-based method, and based on the nanoindentation hardness (H) and elastic modulus (E), the materials' capacity for energy dissipation (E^2/H) and resistance to plastic deformation (H^3/E^2) are analyzed. The relationship between chemical composition, microstructural changes, and mechanical performance is established.

2 Experimental

2.1 Preparation of $Cr_2(Ti_{1-x}V_x)AlC_2$ MAX ceramics

Graphite powder (99.9% purity) was sourced from Alfa Aesar (China) Chemical Co., Ltd., while the other materials, including Cr, Ti, V, and Al, all at 99.9% purity, were obtained from Qinghe Benyu Metal Materials Co., Ltd., China. All powders were used without further purification.

The $Cr_2(Ti_{1-x}V_x)AlC_2$ (x = 0, 0.1, 0.2, 0.3, 0.4, 0.5, and 0.6) ceramics were synthesized via a hot-press sintering technique. The resulting samples were denoted as V0, V0.1, V0.2, V0.3, V0.4, V0.5, and V0.6, corresponding to their respective V solid solution contents. In a typical procedure, the Cr, Ti, V, Al, and C powders were combined in molar proportions of 2 : 1–x : x : 1.4 : 1.9. The atomic ratio of Al to C is 1.4 : 1.9, rather than the ideal 1 : 2. This is because the excess Al compensates for Al loss due to volatilization during high-temperature sintering, thereby preventing the formation of Al-deficient impurity phases. Furthermore, since the use of graphite molds introduces additional C, appropriately reducing the C content minimizes the formation of carbide impurity phases. The mixture was then ball-milled twice for 30 min each under Ar atmosphere using a high-energy ball mill (MSK-SFM-3, Shenzhen Kejing Star Technology Co., Ltd.) with a 30-min interval between cycles. Subsequently, the mixed powder was compacted into a graphite mold with a diameter of 25 mm and sintered by hot pressing under an argon flow. The sintering was conducted in a modified tube furnace (GSL-1700 X, Hefei Kejing Materials Technology Co., Ltd.) under a pressure of 10 MPa. The heating and cooling protocol involved a rate of 10 °C·min^{-1} below 1100 °C, followed by a slower rate of less than 5 °C·min^{-1} above this temperature. Finally, the sintered bulk was sectioned into a semicircular shape, ground sequentially with SiC sandpaper up to 3000 grit, polished, ultrasonically cleaned in anhydrous ethanol, and air-dried.

2.2 Materials characterizations

X-ray diffraction (XRD) patterns were recorded using a diffractometer (D8 ADVANCE, Bruker, 2θ = 5°–120°, step size = 0.02°) [39], followed by Rietveld refinement with GSAS II software to extract lattice parameters and evaluate phase purity [40]. The refinement quality was assessed by the weighted profile R-factor (R_{wp}, < 10%) and goodness-of-fit (GOF, < 2) for all samples. The spherical harmonics function was applied to correct for preferred orientation. The following parameters were refined for all samples: background coefficients (Chebyshev polynomial), lattice parameters, and atomic coordinates [32]. Site occupancy refinement was performed only for the V0.5 and V0.6 samples to assess the distribution of Cr, Ti, and V between the 4*f* and 2*a* sites. For the remaining samples, site occupancies were fixed at their ideal values (Cr fully at the 4*f* Wyckoff site, Ti at the 2*a* Wyckoff site) to avoid overfitting. For V0.5 and V0.6, the occupancies of Cr, Ti, and V at the 4*f* and 2*a* sites were refined iteratively, with constraints that the total occupancy of each site sums to unity and that the isotropic thermal displacement parameters (U_{iso}) of different atoms on the same site were constrained to be equal to reduce parameter correlation and improve stability [40]. The refinement was carried out in an iterative manner: Initial cycles fixed occupancies while refining other parameters, followed by cycles where occupancies were released. A high-vacuum backscattered electron (BSE) probe on a scanning electron microscope (Helios G4 CX, FEI) was used to observe the different phases present in the material, and an energy-dispersive spectrometer was employed to analyze their elemental distribution. The series of $Cr_2(Ti_{1-x}V_x)AlC_2$ (x = 0–0.5) samples were polished and then etched with Keller's reagent (95 mL H_2O, 2.5 mL HNO_3, 1.5 mL HCl, and 1.0 mL HF) for 5 min to reveal grain boundaries. Subsequently, the grain distribution and grain size were observed by scanning electron microscopy (SEM).

$Cr_2(Ti_{0.5}V_{0.5})AlC_2$ thin foil specimens were fabricated using a dual-beam focused ion beam (FIB)/scanning electron microscope (Helios G4 CX, FEI). High-angle annular dark-field scanning transmission electron microscopy (HAADF-STEM) imaging was performed on a transmission electron microscope (Themis Z, FEI), providing atomic-resolution visualization of the Cr, Ti, V, and Al distribution within the lattice. Energy-dispersive X-ray spectroscopy (EDS) mapping and line profile analysis were conducted in conjunction with HAADF-STEM characterization.

2.3 Mechanical tests

After surface polishing and cleaning, the samples underwent Vickers hardness and nanoindentation testing. Vickers hardness was determined using a diamond indenter under a load of 0.5 kgf, held for 10 s. Each sample underwent approximately 15–20 indentation tests to obtain the Vickers hardness of the material. Subsequently, nanoindentation tests were conducted using a Bruker Hysitron nanoindenter, applying a constant load of 10 mN, with at least 10 measurements taken. The Oliver–Pharr method was employed to evaluate the elastic modulus and nanoindentation hardness of the sample [41].

An energy-based approach was simultaneously applied to determine the fracture toughness of the material. The total work (W_{total}) was obtained by integrating the loading curve in the nanoindentation load-displacement curve, while the reversible work (W_{rev}) was derived by integrating the unloading curve, thereby yielding the irreversible work (W_{irrev}) (Eq. (1)) [42]:

$$W_{irrev} = W_{total} - W_{rev} \tag{1}$$

The assumption of irreversible work came only from crack formation (W_{crack}) and plastic deformation of the material (W_{PP}) (Eq. (2)):

$$W_{irrev} = W_{PP} + W_{crack} \tag{2}$$

where W_{PP} represents the work done by the pure plastic deformation of the specimen, while W_{crack} denotes the work done in producing the crack. The purely plastic work (W_{PP}) can be obtained from Eq. (3) [43]:

$$\frac{W_{PP}}{W_{total}} = 1 - \frac{1 - 3\left(\frac{h_p}{h_m}\right)^2 + 2\left(\frac{h_p}{h_m}\right)^3}{1 - \left(\frac{h_p}{h_m}\right)^2} \tag{3}$$

where h_m is the maximum displacement under the maximum load (P_m), and h_p is the indentation depth. This allows calculation of the work done to initiate cracking, W_{crack} (Eq. (2)). Subsequently, the energy-strain release rate (G_c) was calculated using Eq. (4) [44]:

$$G_c = \frac{\partial W_{crack}}{\partial A} = \frac{W_{crack}}{A_m} \tag{4}$$

The contact area (A) at maximum displacement, denoted as A_m, can be calculated as $A_m = P_m/H$, where H represents the nanoindentation hardness, and P_m denotes the maximum load. Subsequently, G_c was computed. For each sample group, three points were selected for repeated experiments, ultimately yielding K_{IC} of the sample (Eq. (5)) [42]:

$$K_{IC} = \varnothing\sqrt{EG_c} \tag{5}$$

where $\varnothing$ represents the calibration factor, derived from the fracture toughness (K'_{IC} = 6.08 MPa·m$^{1/2}$) measured for a reported Cr_2TiAlC_2 specimen using the single-edge notched beam (SENB) method and the fracture toughness (K_{IC}^{energy}, $\varnothing$ = 1) calculated using the uncalibrated energy method [23]. The calculation formula is $\varnothing = K'_{IC}/K_{IC}^{energy}$. In this paper, $\varnothing$ was taken as 2.62 and then applied to all samples to obtain the calibrated K_{IC} values.

2.4 Computational methods

First-principles calculations were performed using the Vienna *ab initio* simulation package (VASP) based on density functional theory (DFT) [45]. Electron–ion interactions were described using the projected augmented wave (PAW) method, and the exchange–correlation energy was treated using the Perdew–Burke–Ernzerhof (PBE) functional under the generalized gradient approximation (GGA), with the plane-wave cutoff set at 600 eV [46,47]. To investigate the effect of different atomic configurations on the system's stability, four structural models were constructed: $Cr_2(Ti_{0.75}V_{0.25})AlC_2$, $(Cr_{0.75}V_{0.25})_2(Ti_{0.75}V_{0.25})AlC_2$, $(Cr_{0.75}Ti_{0.25})_2(Ti_{0.75}V_{0.25})AlC_2$, and $(Cr_{0.5}Ti_{0.25}V_{0.25})_2(Ti_{0.5}V_{0.25}Cr_{0.25})AlC_2$, which were named M1, M2, M3, and M4, respectively. All models were generated using the special quasi-random structure (SQS) method based on a 2 × 2 × 1 supercell (48 atoms, corresponding to 8 chemical units), with Cr_2TiAlC_2 as the initial structure [48]. Different site occupancy distributions were achieved in each model through stepwise atomic substitution: M1 ($Cr_2(Ti_{0.75}V_{0.25})AlC_2$) replaced 1/4 of the Ti atoms at the 2*a* sites with V, resulting in 6 Ti and 2 V atoms at the 2*a* sites; M2 ($(Cr_{0.75}V_{0.25})_2(Ti_{0.75}V_{0.25})AlC_2$) further replaced one-quarter of the Cr atoms at the 4*f* sites with V based on M1, resulting in 12 Cr and 4 V atoms at the 4*f* sites; M3 ($(Cr_{0.75}Ti_{0.25})_2(Ti_{0.75}V_{0.25})AlC_2$) was derived from M1 by further replacing one-quarter of the Cr atoms at the 4*f* sites with Ti, resulting in 12 Cr and 4 Ti atoms at the 4*f* sites; and M4 ($(Cr_{0.5}Ti_{0.25}V_{0.25})_2(Ti_{0.5}V_{0.25}Cr_{0.25})AlC_2$) involved multiple substitutions at the 4*f* and 2*a* sites based on M1, achieving a high degree of mixing of Cr, Ti, and V. Ultimately, the 4*f* sites contained 8 Cr, 4 Ti, and 4 V, while the 2*a* sites contained 4 Ti, 2 V, and 2 Cr. The centered gamma scheme was adopted for *k*-point sampling in the Brillouin zone, with the *k*-point mesh set to 9 × 9 × 2 [48]. Geometric optimization was performed using the conjugate gradient method, with a convergence criterion set such that the force per atom was less than 0.02 eV·Å^{-1}, and the energy change between two consecutive steps was less than 1.0×10^{-6} eV·atom^{-1}. The formation energies were calculated using $E_{form} = (E_{total} - \sum_i n_i E_i)/N$, where E_{total} is the total energy of the supercell; n_i is the number of atoms of element *i*; E_i is the energy of the corresponding elemental reference state; N is the total number of atoms in the supercell [49,50]. The resulting formation energy is expressed in eV·atom^{-1}.

3 Results and discussion

3.1 The structure of $Cr_2(Ti_{1-x}V_x)AlC_2$ MAX ceramics

The effect of sintering temperature on the formation yield of the target $Cr_2(Ti_{1-x}V_x)AlC_2$ MAX phase was first evaluated using $Cr_2(Ti_{0.5}V_{0.5})AlC_2$ samples. As shown in Fig. S1 in the Electronic Supplementary Material (ESM), the $Cr_2(Ti_{0.5}V_{0.5})AlC_2$ sample exhibits poor phase purity during sintering at 1365 °C, with a significant presence of miscellaneous phases. After sintering at 1400 °C, the purity of the Cr_2TiAlC_2 phase (312 phase) increased, exhibiting good crystallinity. However, when the heat treatment temperature was further elevated to 1450 and 1500 °C, the peak intensity corresponding to the 312 phase weakened again, indicating possible overfiring. Therefore, a sintering temperature of 1400 °C was selected to prepare $Cr_2(Ti_{1-x}V_x)AlC_2$ MAX phase

ceramics containing different V contents. Preliminary structural characterization of the $Cr_2(Ti_{1-x}V_x)AlC_2$ series samples was performed via XRD Rietveld refinement [40]. Figure 1 presents the experimental data (black curve), the Rietveld-fitted results (red curve), and the difference between the two (green curve). All samples predominantly exhibited the high-purity 312 phase, with sample purity higher than 95% when the V content exceeded 0.2. The highest purity was achieved in the V0.2 sample, where the 312 phase purity reached 98.2%. Additionally, due to the excess Al powder added during preparation, all samples contained varying proportions of Al_2O_3 impurity phases, with the corresponding contents shown in Table 1. The V0 sample also included partial Cr_2AlC 211 MAX phase (3.6%) and TiC phase (2.4%). The V0.1 and V0.2 samples contained residual transition metal carbide TiC phases at 2.5% and 1.3%, respectively. When the V ratio increased from 0.3 to 0.5, Cr_3C_2 replaced TiC as the carbide impurity phase, with Cr_3C_2 contents of 2.3%, 3.4%, and 0.8%, respectively.

Atomic composition analysis of the $Cr_2(Ti_{0.5}V_{0.5})AlC_2$ sample via XRD Rietveld refinement confirms Cr's stable occupation at the 4*f* Wyckoff site, while Ti and V exhibit solid solution at the 2*a* Wyckoff site (Table S1 in the ESM). This demonstrates that V's solid solution maintains the material's original out-of-plane chemically ordered structure. It should be noted that for elements with similar atomic numbers (Cr, Ti, and V), XRD Rietveld refinement cannot provide precise atomic occupancy values. To further validate the site occupancy assignment for the V0.5

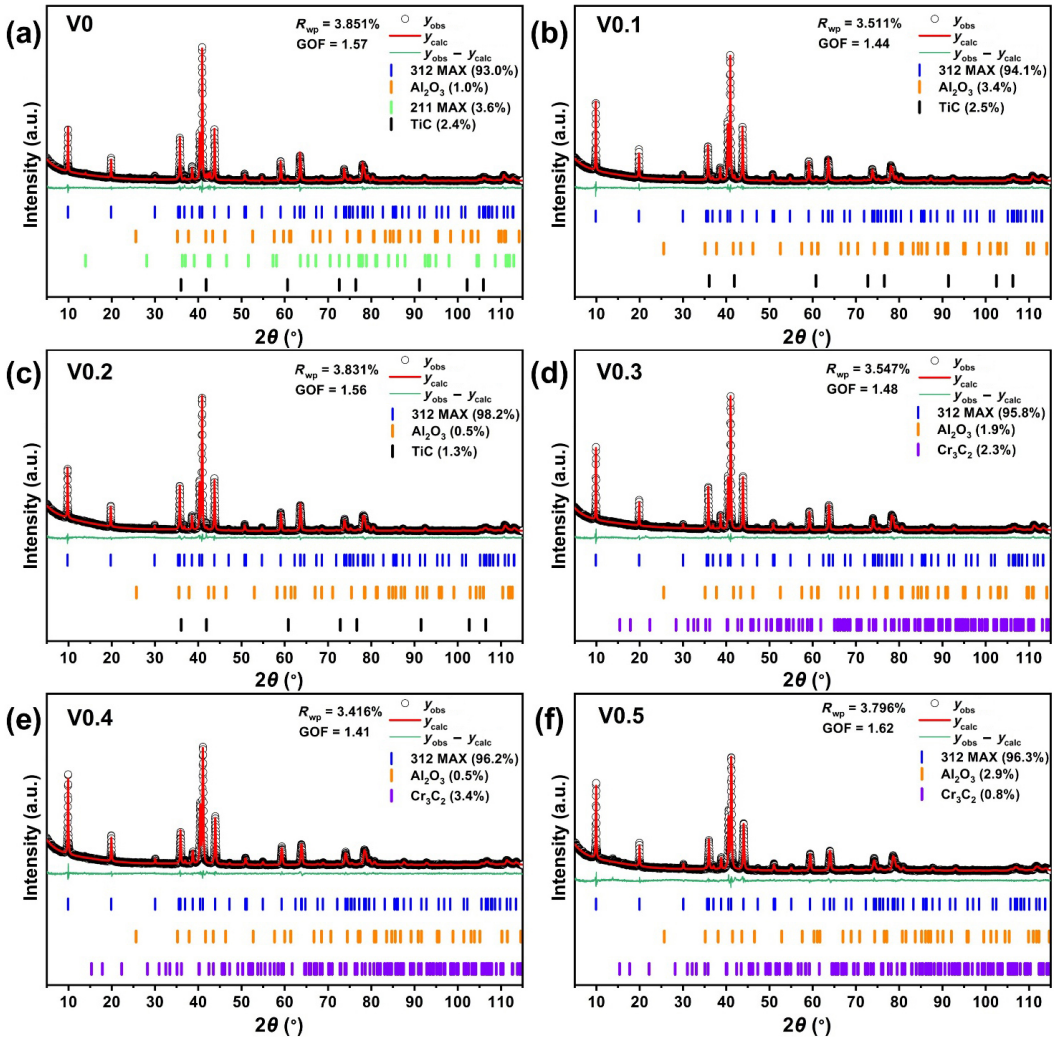


Fig. 1 XRD Rietveld refinement results of (a) V0, (b) V0.1, (c) V0.2, (d) V0.3, (e) V0.4, and (f) V0.5.

Table 1 Phase composition of the $Cr_2(Ti_{1-x}V_x)AlC_2$ MAXs (Unit: wt%)

Sample	312 MAX	Al_2O_3	211 MAX	TiC	Cr_3C_2
V0	93.0	1.0	3.6	2.4	—
V0.1	94.1	3.4	—	2.5	—
V0.2	98.2	0.5	—	1.3	—
V0.3	95.8	1.9	—	—	2.3
V0.4	96.2	0.5	—	—	3.4
V0.5	96.3	2.9	—	—	0.8

sample, multiple Rietveld refinements were performed using different site-occupancy models (Table S2 in the ESM). Three mixed-occupancy models were tested: R1 (Cr and V at 4*f* sites, Ti and V at 2*a* sites); R2 (Cr, Ti, and V at 4*f* sites, Ti and V at 2*a* sites); and R3 (Cr, Ti, and V at both 4*f* and 2*a* sites). All three models yielded physically unreasonable negative occupancies, with R_{wp} values of 4.040%, 5.501%, and 4.783% and GOF values of 1.73, 2.36, and 2.05, respectively, all of which were higher than those of the ordered model shown in Fig. 1(f) (R_{wp} = 3.796%, GOF = 1.62). The ordered model gave a superior fit without negative occupancies, confirming that the V0.5 sample retains an out-of-plane ordered structure (Cr at the 4*f* site, Ti and V at the 2*a* sites). Therefore, the values in Table S1 in the ESM should be regarded as semiquantitative indicators, primarily used to determine whether a specific element occupies a particular site (e.g., whether Ti or V occupies the 4*f* site), rather than representing exact proportions. Consequently, the term $Cr_2(Ti_{1-x}V_x)AlC_2$ is consistently used throughout the text to describe the V incorporation ratio.

After locally enlarging and stacking the XRD patterns of the synthesized $Cr_2(Ti_{1-x}V_x)AlC_2$ samples, it can be observed that all samples exhibit consistent diffraction peak shapes. Simultaneously, with increasing V doping ratio, the XRD diffraction peaks of the resulting samples shift collectively toward higher angles, indicating continuous lattice contraction (Fig. 2(a)). The detailed lattice parameters obtained after refinement for the six samples are plotted in Fig. 2(b) and summarized in Table 2.

As shown in Fig. 2(b), both the *a* and *c* lattice constants of the $Cr_2(Ti_{1-x}V_x)AlC_2$ samples exhibit a monotonically decreasing trend as the V doping ratio increases from 0.1 to 0.5. Specifically, the *a*-axis parameter contracted from 2.92631 (x = 0) to 2.90818 Å (x = 0.5), representing a cumulative contraction of approximately 0.62%. The *c*-axis parameter decreased from 17.8715 to 17.7870 Å, with a cumulative contraction of approximately 0.47%. This trend is consistent with the fact that the atomic radius of V is smaller than that of Ti, further confirming the solid solution of V and the gradient variation in its concentration [51,52].

To analyze the distribution of various phases within the prepared samples, BSE images were probed on a scanning electron microscope to observe the different phases present in the materials. Additionally, elemental distribution analysis was conducted on the distinct phase regions of the six prepared MAX specimens using an accompanying energy-dispersive spectrometer. From the BSE image of the V0 sample in Fig. 3(a), three distinct contrast regions can be observed in the material: black, gray, and light gray. The EDS spectrum of the V0 sample reveals a uniform distribution of Cr, Ti, Al, C, and O elements in the light gray region. In contrast, the black region exhibits segregation of Al and O elements, with overlapping energy spectra for Al and O. The gray region shows enrichment of Ti and C elements while lacking Cr. Preliminary identification suggests that the light gray phase is the matrix Cr_2TiAlC_2, the black phase is aluminum oxide, and the gray phase is titanium carbide [53]. Furthermore, EDS point scanning analysis was conducted on three distinct phase regions within the V0 sample. Figure 3(b) shows the BSE image at high magnification and the corresponding locations for EDS point analysis of the V0 sample.

The EDS point scan data are presented in Table 3. The atomic ratios of Cr, Ti, and Al in the light gray region (spectrum 1) closely match the 2 : 1 : 1 stoichiometric ratio in its chemical formula, further confirming it as the matrix Cr_2TiAlC_2. Simultaneously, the increased Al and O content in the black region (spectrum 2) and the sharp rise in Ti and C content in the gray region (spectrum 3), combined with refined XRD data, indicate two impurity phases: Al_2O_3 and TiC [54]. Additionally, Spectrum 4 represents a small, darker region within the matrix where the atomic ratio of transition metal M to Al is close to 2 : 1. Analysis based on refined XRD results confirms this region as a 211 MAX impurity phase. Figures 3(c)–3(f) show the BSE images of the V0.1 and V0.2 samples. Similar to the V0 sample, three contrast regions, light gray (spectrum 1), black (spectrum 2), and gray regions (spectrum 3), can be observed. The light gray phase exhibits a uniform distribution of Cr, Ti, V, Al, C, and O elements, indicating successful incorporation of V and formation of the matrix 312 MAX phase. Meanwhile, the black phase exhibits Al and O segregation, suggesting an Al_2O_3 impurity

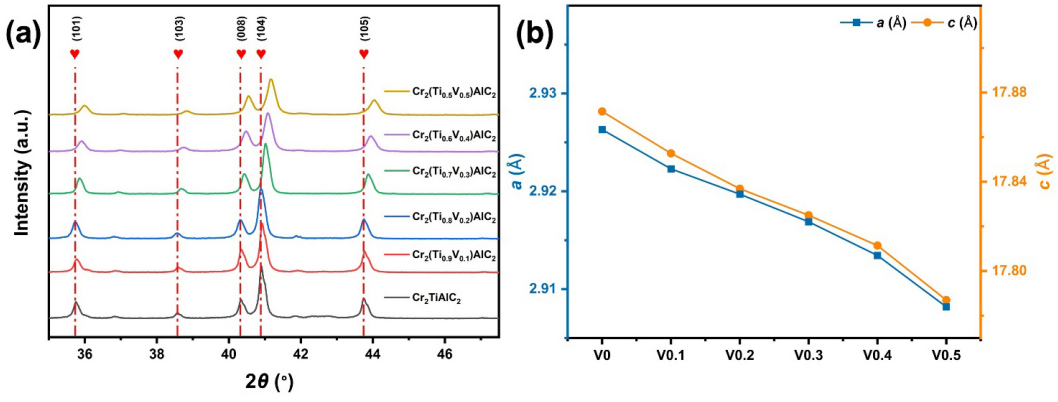


Fig. 2 (a) Partial enlarged and stacked XRD patterns and (b) unit cell parameter diagram of the $Cr_2(Ti_{1-x}V_x)AlC_2$ samples.

Table 2 Lattice parameters of the $Cr_2(Ti_{1-x}V_x)AlC_2$ series samples obtained through Rietveld refinement

Parameter	V0	V0.1	V0.2	V0.3	V0.4	V0.5
Crystal system	Hexagonal	Hexagonal	Hexagonal	Hexagonal	Hexagonal	Hexagonal
Space group	$P6_3/mmc$	$P6_3/mmc$	$P6_3/mmc$	$P6_3/mmc$	$P6_3/mmc$	$P6_3/mmc$
a (Å)	2.92631	2.92229	2.91970	2.91688	2.91344	2.90818
c (Å)	17.8715	17.8527	17.8369	17.8250	17.8114	17.7870
V (Å^3)	132.536	132.033	131.682	131.340	130.930	130.279

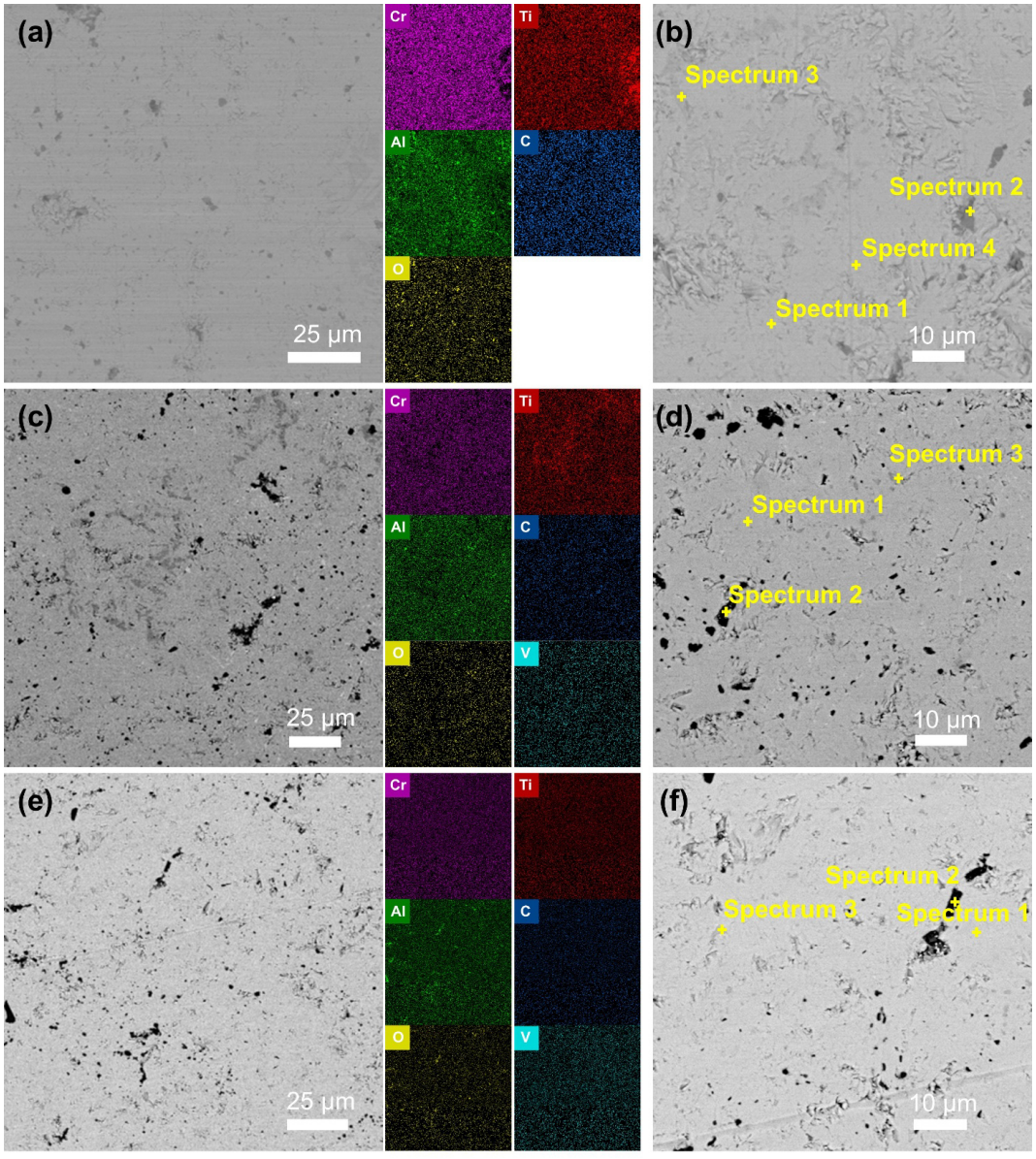


Fig. 3 BSE images accompanied by EDS elemental maps for (a) Cr_2TiAlC_2, (c) $Cr_2(Ti_{0.9}V_{0.1})AlC_2$, and (e) $Cr_2(Ti_{0.8}V_{0.2})AlC_2$. Enlarged BSE images of (b) Cr_2TiAlC_2, (d) $Cr_2(Ti_{0.9}V_{0.1})AlC_2$, and (f) $Cr_2(Ti_{0.8}V_{0.2})AlC_2$ and the sites selected for EDS point analysis.

Table 3 Atomic percentage contents of elements on the surfaces of Cr_2TiAlC_2 (Unit: at%)

	Cr	Ti	Al	C	O
Spectrum 1	29.38	14.98	14.27	39.45	1.91
Spectrum 2	0.21	0.15	35.58	7.97	56.09
Spectrum 3	5.29	41.08	2.66	50.03	0.94
Spectrum 4	27.91	12.18	20.26	34.31	5.34

phase. Unlike the V0 sample, however, the gray regions in the V0.1 and V0.2 samples show no Cr deficiency. To further investigate the phase composition of these two samples, EDS point analysis was performed on different regions, with specific elemental atomic ratios shown in Tables S3 and S4 in the ESM. Spot scan results indicate that the gray regions in both samples contain abundant transition metal elements and C. Combined with refined XRD results, this impurity phase is likely an MC carbide containing solid-solution transition metal elements [38].

Figure 4 reveals that the V0.3, V0.4, and V0.5 samples primarily exhibit three phases. Similar to previous samples, black and light gray regions are present. The black regions (spectrum 2) show clustering of Al and O elements, identified as Al_2O_3 impurity phases. The light gray regions (spectrum 1) feature a uniform distribution of Cr, Ti, V, Al, C, and O elements, corresponding to the matrix 312 MAX phase. Distinctively, all three samples exhibit a white impurity phase characterized by Cr and C element segregation, preliminarily identified as chromium carbide. Subsequently, EDS point scanning analysis was performed on the three samples, with the scanned regions shown in Figs. 4(b), 4(d), and 4(f). The white regions (spectrum 3) in all three samples exhibited abrupt increases in C and Cr content (as shown in

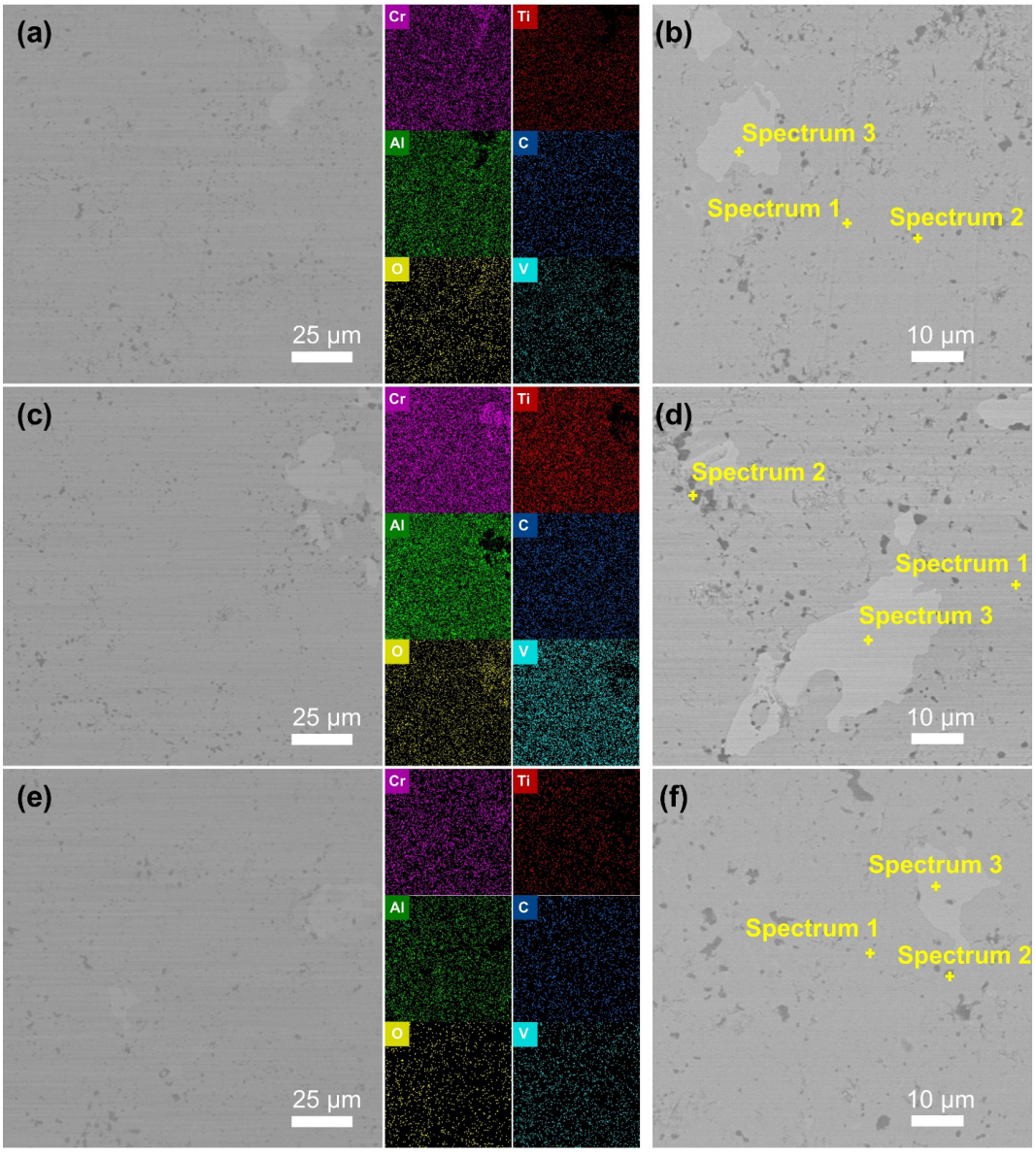


Fig. 4 BSE images accompanied by EDS elemental maps for (a) $Cr_2(Ti_{0.7}V_{0.3})AlC_2$, (c) $Cr_2(Ti_{0.6}V_{0.4})AlC_2$, and (e) $Cr_2(Ti_{0.5}V_{0.5})AlC_2$. Enlarged BSE images of (b) $Cr_2(Ti_{0.7}V_{0.3})AlC_2$, (d) $Cr_2(Ti_{0.6}V_{0.4})AlC$, and (f) $Cr_2(Ti_{0.5}V_{0.5})AlC_2$ and the sites selected for EDS point analysis.

Tables S5 and S6 in the ESM and Table 4). Combined with the refined XRD results, the white impurity phase was identified as Cr_3C_2. Subsequently, SEM and EDS line scanning analysis of the V0.5 sample cross-section yielded the results shown in Fig. S2 in the ESM, further confirming the macroscopic homogeneity of the prepared samples. Analysis of the phase composition in the six prepared samples reveals that as the V content increases, the competing carbide phase shifts from TiC to Cr_3C_2.

The phase transition from TiC to Cr_3C_2 is primarily thermodynamically driven. As the degree of V substitution for Ti increases, the reactivity of Ti decreases [55]. The chemical environment of the system becomes more favorable for the formation of Cr_3C_2, causing the thermodynamically stable region of the system to gradually shift from TiC to Cr_3C_2, consistent with the results of computational simulations (where the competing phase for Cr_2TiAlC_2 is TiC, while the competing phase for Cr_2VAlC_2 is Cr_3C_2) [25]. The microstructure of the corroded $Cr_2(Ti_{1-x}V_x)AlC_2$ (x = 0–0.5) samples was examined using the BSE imaging mode of a scanning electron microscope. The sizes of the grains clearly visible in the BSE images were then measured and statistically analyzed using Nano Measurer image analysis software. The results are shown in Fig. S3 in the ESM. The analysis indicates that the average grain size gradually decreases with increasing V content, suggesting a grain refinement effect. Specifically, the average grain size of the V0 sample was 9.11 μm, whereas that of the V0.5 sample decreased to 6.33 μm, representing a reduction of approximately 30.52%.

Table 4 Atomic percentage contents of elements on surfaces of $Cr_2(Ti_{0.5}V_{0.5})AlC_2$ (Unit: at%)

	Cr	Ti	V	Al	C	O
Spectrum 1	22.60	6.70	6.04	10.92	52.74	1.00
Spectrum 2	0.85	0.20	0.24	29.38	24.31	45.01
Spectrum 3	42.17	0.42	2.16	0.78	51.83	2.64

3.2 Chemical ordering in $Cr_2(Ti_{0.5}V_{0.5})AlC_2$

To probe the elemental distribution of Cr, Ti, and V throughout the lattice structure, the V0.5 sample was analyzed by HAADF aberration-corrected STEM combined with EDS. Figure 5(a)

displays the selected area electron diffraction (SAED) pattern obtained using an electron beam parallel to the [11$\bar{2}$0] direction [56]. Hexagonal electron diffraction features characteristic of the $Cr_2(Ti_{0.5}V_{0.5})AlC_2$ material are observed, consistent with the basic structure of MAX phase materials [32]. Subsequently, the HAADF-STEM image of the $Cr_2(Ti_{0.5}V_{0.5})AlC_2$ sample (Fig. 5(b)) reveals a typical layered structure with three atomic layers in thickness, observed along the <11$\bar{2}$0> crystal zone axis. Furthermore, the corresponding EDS mapping revealed distinct enrichment of Cr, Ti, and Al atoms in different layers, exhibiting an out-of-plane chemical ordering similar to that observed in Cr_2TiAlC_2 [21].

To further illustrate the ordered atomic distribution span between layers, line-scan EDS was carried out along the *c*-axis direction (Fig. 5(b)). As shown in Fig. 5(c), Al layers alternated in the interlayer regions of the M_3C_2 slabs, while Cr and Ti distributions were distinctly separated, corresponding to the 4*f* and 2*a* Wyckoff sites in the lattice, respectively [29,36]. V atoms exhibited a highly consistent distribution with Ti atoms, interleaving between two Cr layers, indicating that a solid solution formed between V and Ti at the 2*a* Wyckoff site. Within one unit cell (yellow region in the figure), atoms are ordered in the sequence Al–Cr–(Ti,V)–Cr–Al. The alternating distribution of Ti and V between two Cr layers further confirms successful V doping and the formation of a solid solution between V and Ti at the 2*a* Wyckoff site. However, due to electron beam irradiation damage that MAX phase materials are prone to during prolonged HAADF-STEM imaging, crystallinity decreases and atomic displacement may occur, leading to a certain degree of signal confusion in the EDS line distribution (e.g., a small amount of V signal appearing in the Al layer or a small amount of Ti signal appearing in the outer layer) [57,58]. Although some signal overlap exists, the core trend of Cr enrichment in the outer layer and Ti/V enrichment in the inner layer is clear, forming a fundamental distinction from the mixed distribution in $(CrTiV)_3AlC_2$ (identified as having a disordered structure) [38]. Combining the atomic site occupancy ratios of $Cr_2(Ti_{0.5}V_{0.5})AlC_2$ derived from XRD Rietveld refinement (Table S1 in the ESM), it is concluded that V incorporation enables solid solution formation between V and Ti at the 2*a* Wyckoff site, building upon the original out-of-plane chemically ordered layered structure [59].

In the previously reported $(CrTiV)_3AlC_2$ MAX phase, V atoms form solid solutions with both Cr and Ti atoms in the lattice, occupying both the 4*f* and 2*a* Wyckoff sites [38]. In this study, by adjusting the V atom stoichiometry, the V solid solution can be confined to the 2*a* Wyckoff site. Vegard's law states that in continuous solid solutions, the lattice constant of the unit cell is linearly proportional to the solute atom concentration [60]. Therefore, to elucidate the control mechanism of the atomic ratio of V on this solid solution behavior, the predicted lines of Vegard's law were plotted in Figs. 6(a) and 6(b) based on the lattice parameters of Cr_2TiAlC_2 and $(CrV)_3AlC_2$ (Table S1 in the ESM) [37,61]. Analysis of lattice parameters for the $Cr_2(Ti_{1-x}V_x)AlC_2$ (x = 0–0.5) series in conjunction with Vegard's prediction line reveals a linear decrease in lattice parameters, consistent with Vegard's prediction trend [62]. This indicates an uncollapsed structure, i.e., an out-of-plane chemically ordered structure, within the composition range. It is worth noting that the *c*-axis lattice parameter exhibits a slight negative deviation from the values predicted by Vegard's law (Fig. 6(b)), which is attributed to the smaller V radius and anisotropic contraction along the *c*-axis, a direction that is more sensitive to atomic substitutions in the M layer [61,63]. Similar deviations have been

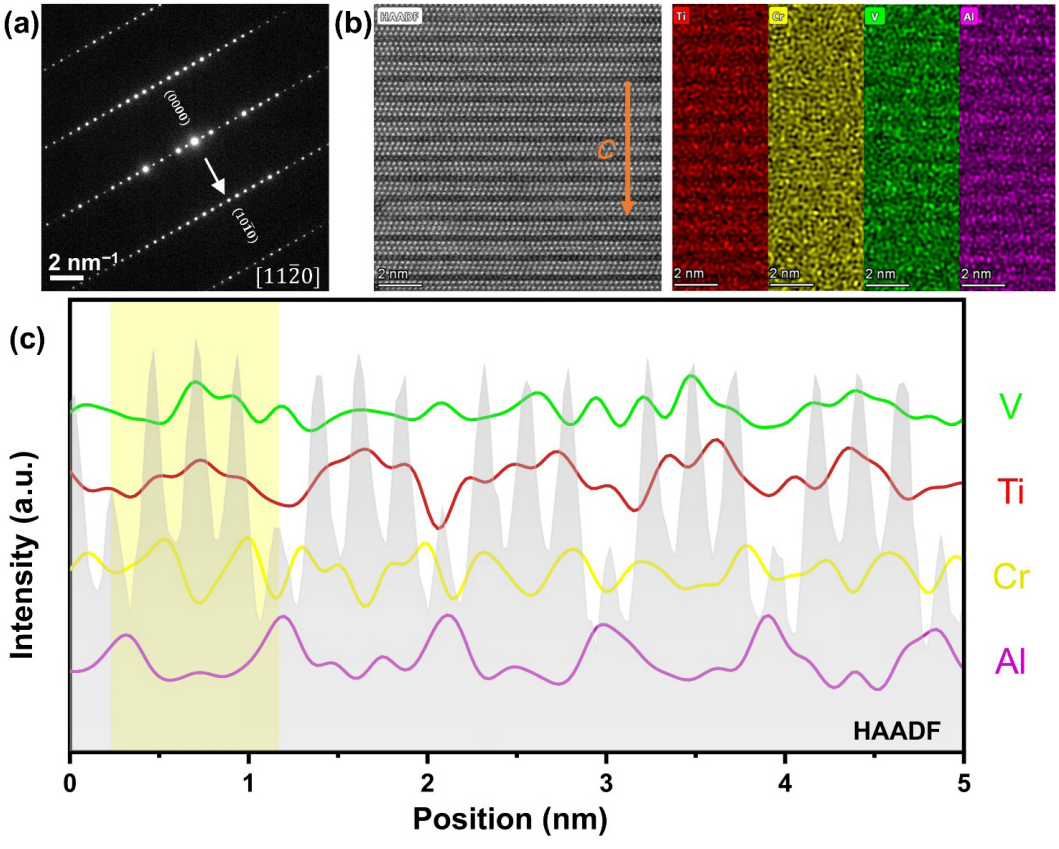


Fig. 5 $Cr_2(Ti_{0.5}V_{0.5})AlC_2$ sample: (a) SAED pattern with electron beam parallel to the [11$\bar{2}$0] direction, (b) HAADF-STEM image and EDS elemental distribution map, and (c) line-scan EDS along the *c*-axis direction in (b).

observed in other MAX phase solid solutions, and such phenomena are typically associated with nonlinear distortion of the M_6X octahedra [64]. At the same time, $(CrV)_3AlC_2$ exists in a partially solid-solved state, which means that the unit cell parameters at the two endpoints used for Vegard's law fit are not fully ordered [37]. This limitation can also cause the theoretically predicted curve to deviate from the actual experimental observations. Therefore, this deviation falls within the typical fluctuation range for MAX phase solid solutions and does not violate Vegard's law. Moreover, a $Cr_2(Ti_{0.4}V_{0.6})AlC_2$ sample was also synthesized. As analyzed via XRD Rietveld refinement (Fig. S4 and Table S1 in the ESM), the phase purity of the $Cr_2(Ti_{0.4}V_{0.6})AlC_2$ sample significantly decreases, with only 67.0% 312 phase remaining. When plotting the lattice parameters of $Cr_2(Ti_{0.4}V_{0.6})AlC_2$ together with $Cr_2(Ti_{1-x}V_x)AlC_2$ (x = 0–0.5) in Fig. 6, both the *a*-axis and *c*-axis lattice parameters exhibit positive deviations according to Vegard's prediction line, indicating an internal structure evolution, e.g., an ordered–disordered transition in the crystal structure [65]. To further validate this inference, we performed Rietveld refinements for the V0.6 sample using both an ordered model R4 (Cr exclusively at 4*f* site, Ti and V at 2*a* sites) and a mixed-occupancy model (Cr, Ti, and V at 4*f* sites, Ti and V at 2*a* sites). The results are summarized in Tables S1 and S2 in the ESM. The ordered model produced physically unreasonable occupancies (Ti > 1, V negative), with R_{wp} = 3.293% and GOF = 1.28 (Table S2 in the ESM). In contrast, the mixed-occupancy model yielded all occupancies within physically reasonable ranges (Table S1 in the ESM), revealing that V and Ti atoms partially occupy the 4*f* sites originally belonging to Cr, while Ti and V coexist at the 2*a* sites. This confirms that the V0.6 sample adopts a disordered mixed-occupancy structure. This site occupancy pattern is nearly identical to that of the $(CrTiV)_3AlC_2$ MAX phase, which has been directly characterized as a chemically disordered state, indicating that the out-of-plane chemical order in the V0.6 sample has also been disrupted [38].

At the same time, to further verify the relationship between atomic site selectivity and the observed order–disorder phase transition, we constructed four structural models based on the $Cr_2(Ti_{1-x}V_x)AlC_2$ system, each featuring a different atomic arrangement (Fig. S5 in the ESM): $Cr_2(Ti_{0.75}V_{0.25})AlC_2$, $(Cr_{0.75}V_{0.25})_2(Ti_{0.75}V_{0.25})AlC_2$, $(Cr_{0.75}Ti_{0.25})_2(Ti_{0.75}V_{0.25})AlC_2$, and $(Cr_{0.5}Ti_{0.25}V_{0.25})_2(Ti_{0.5}V_{0.25}Cr_{0.25})AlC_2$. Among these models, M1 (ordered structure, with V occupying only the 2*a* sites) represents the atomic configuration of the V0.1–V0.5 samples, in which out-of-plane chemical order is preserved. In contrast, M2, M3, and M4 (characterized by a gradual increase in the degree of mixed occupancy of the 4*f* and 2*a* sites) correspond to the disordered structure observed in the V0.6 sample, where V and Ti atoms partially occupy the 4*f* sites. As shown in Figs. 6(c) and 6(d), the lattice parameters and formation energy were calculated, and the results for the lattice constants are summarized in Table S7 in the ESM.

When V forms a solid solution exclusively with Ti at the 2*a* Wyckoff site (M1), the lattice parameters decrease relative to those of Cr_2TiAlC_2, which is consistent with the predicted curve and experimental data from Vegard's law (when the V solute content is within the solid solution threshold, the lattice parameters gradually decrease with increasing V solute content) [66]. At the same time, as the degree of atomic mixing in the system increases (M1–M4), the lattice parameters gradually increase, which is consistent with the positive deviation from the V0.6 sample after exceeding the solubility threshold. Therefore, by comparing crystal structure models with different atomic arrangements, the above conclusions can be further corroborated: When $x \le 0.5$, V atoms preferentially occupy the 2*a* sites, maintaining an out-of-plane ordered structure, and the lattice parameters follow Vegard's law, showing a gradual decrease with increasing vanadium content; when $x > 0.5$, the intensification of atomic mixing triggers an order–disorder phase transition, and the changes in the system's lattice parameters deviate from Vegard's law. Therefore, regulating

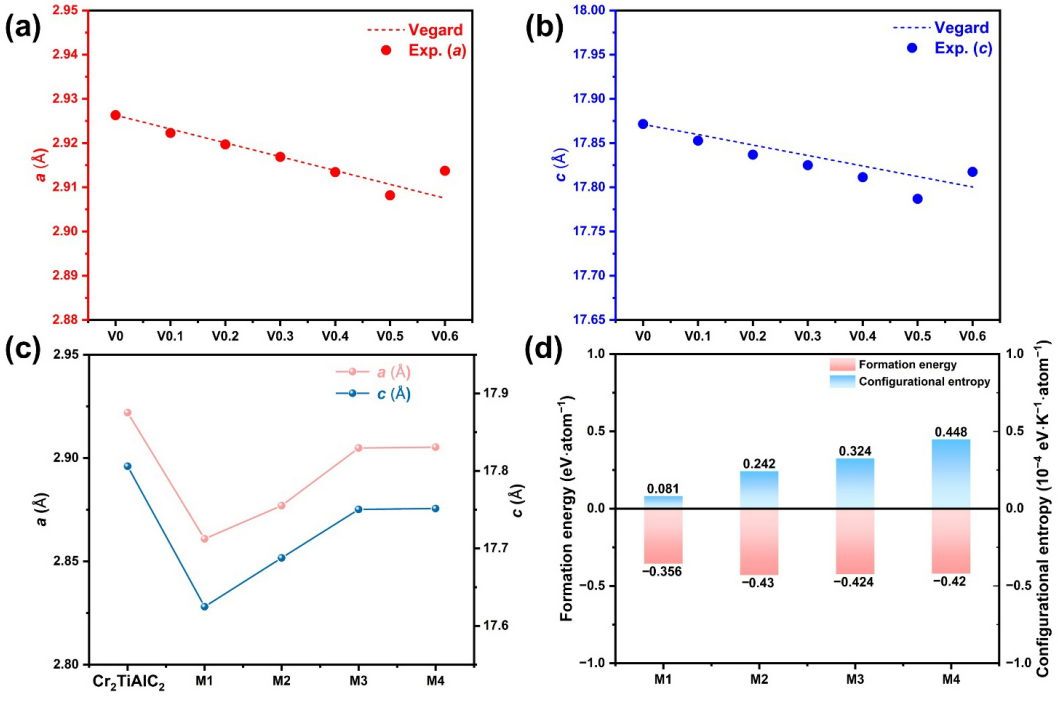


Fig. 6 (a) *a*-axis and (b) *c*-axis lattice parameters predicted curves of $Cr_2(Ti_{1-x}V_x)AlC_2$ (x = 0–0.6) samples based on Vegard's law. The dashed line represents the prediction based on Vegard's law, and the data points represent the experimental results. (c) The lattice parameters of Cr_2TiAlC_2, M1, M2, M3, and M4. (d) Formation energy and configurational entropy of M1, M2, M3, and M4.

V content enables effective control over the atomic occupancy order in MAX phase materials, providing crucial insights for microstructure design and performance optimization.

To further analyze the key factors and intrinsic mechanisms underlying this order–disorder transition, we investigated the influence of configurational entropy [32,33]. Using a sublattice model, we calculated the configurational entropy for the four structural models M1–M4 [67]. The specific calculation formula is Eq. (6):

$$S_{sL}^{\text{config}} = \frac{-R\sum_s\sum_i a^s X_i^s \ln X_i^s}{\sum_s a^s} \quad (6)$$

In Eq. (6), R is the ideal gas constant, a^s is the number of sites on the s sublattice, and X_i^s is the fraction of element species i randomly distributed on the s sublattice, or the site fraction [67]. The unit of S_{sL}^{config} is J·K^{-1}·mol of atoms^{-1} [32]. Based on the constructed M1–M4 structural models, the configurational entropy of each configuration was calculated, and the unit of the configurational entropy was converted to eV·K^{-1}·atom^{-1} using the conversion factor 1 eV·K^{-1}·atom^{-1} = 96,485 J·K^{-1}·mol^{-1} (as shown in Fig. 6(d)). Through comprehensive analysis of the configurational entropy and formation energy data, we attribute this order–disorder transition to the synergistic effect of increased configurational entropy and decreased formation energy. When the V content is low ($x \le 0.5$), V atoms preferentially form a solid solution with Ti atoms at the 2*a* sites, maintaining the ordered stacking structure of Al–Cr-(Ti,V)-Cr–Al. At the same time, the lattice parameters decrease linearly with increasing V content (strictly following Vegard's law), indicating the stable existence of an out-of-plane chemically ordered structure [64,65]. Since the 2*a* sites are far from saturated, the lattice distortion energy is small and insufficient to drive atomic migration. Furthermore, the configurational entropy of the ordered structure (e.g., the M1 structure) is only approximately 8.1×10^{-6} eV·K^{-1}·atom^{-1}. The limited high-temperature entropy gain is insufficient to overcome the energy barrier between the ordered configuration and the mixed-occupancy state. Therefore, entropy-driven mechanisms also cannot trigger a structural transformation [33]. When the V content exceeds the solid solubility threshold ($x > 0.5$), the 2*a* site becomes supersaturated, and the lattice distortion energy accumulates sharply. DFT calculations show that the formation energy of the mixed occupancy configuration M2 (V occupies both 2*a* and 4*f* sites simultaneously) is −0.43 eV·atom^{-1}, which is markedly lower than that of the ordered configuration M1 (V occupies only the 2*a* site, −0.356 eV·atom^{-1}). This indicates that when V exceeds the solid-solution limit, it tends to shift toward the 4*f* sites, forming a thermodynamically more stable disordered structure [18]. At the same time, the configurational entropy of the mixed-site structures (M2–M4) increases significantly, far exceeding that of the ordered structure M1 (from 8.1×10^{-6} to 4.48×10^{-5} eV·K^{-1}·atom^{-1}). The decrease in formation energy provides the thermodynamic driving force for the disordered structure, while the increase in entropy further stabilizes this disordered state at high temperatures [32,33]. These two factors drive the order–disorder transition.

3.3 Mechanical properties of the MAXs

Further experimental evaluation of the mechanical properties was conducted on the prepared $Cr_2(Ti_{1-x}V_x)AlC_2$ (x = 0–0.5) samples. Nanoindentation testing, owing to its high resolution, can be employed to determine micromechanical properties while being minimally affected by heterogeneous phases. Figures 7(a)–7(f) present the displacement-load curves for all six samples during identical loading, holding, and unloading phases. These curves demonstrate similar elastic-plastic deformation, creep, and recovery responses under consistent loading conditions [68]. The loading phase curves for all six samples are nearly superimposed and exhibit low slopes, visually indicating that the tested materials possess low and comparable elastic moduli. During the constant-load holding phase, all curves exhibit a characteristic increase in displacement over time, indicating creep deformation in the material. The initial stage of the unloading curve is extremely steep, revealing high contact stiffness between the indenter and the material. Furthermore, after complete unloading, the displacement does not return to zero. The residual displacement originates from permanent plastic deformation generated during loading and creep deformation accumulated during the holding phase.

Figure 7(g) summarizes the effective E and H of six 312 MAX phases obtained from nanoindentation, as determined by the Oliver–Pharr method [51]. When the V addition ratio was below 0.3, E showed no significant change. However, when the V addition ratio exceeded 0.4, E increased markedly; the nanoindentation hardness gradually increased with increasing V doping ratio. Among these, the V0.5 sample exhibited the highest values for both E (212.48±10.78 GPa) and H (11.56±1.21 GPa), representing increases of approximately 11.6% and 16.4%, respectively, compared to the V0 sample (E = 190.31±12.86 GPa, H = 9.93±1.37 GPa). Microhardness testing of the $Cr_2(Ti_{1-x}V_x)AlC_2$ (x = 0–0.5) series samples was conducted using a Vickers hardness tester.

As shown in Fig. 7(h), the trend in microhardness aligns with that of nanoindentation hardness, with H_v gradually increasing with increasing V content (Table 5). The V0.5 sample exhibited the highest H_v (6.68±0.11 GPa), representing an approximately 35.2% increase compared to the V0 sample (H_v = 4.94±0.12 GPa). Compared to the nanoindentation hardness, the increase in the Vickers hardness is more pronounced. This is due to differences in the scales of the two tests: Nanoindentation primarily measures the intrinsic hardness of the grain, whereas Vickers hardness is more susceptible to the influence of grain boundaries and impurity phases (TiC or Cr_3C_2) [51]. Additionally, grain refinement caused by V dissolution can provide grain boundary strengthening [17]. The combined effect of these two factors results in a steeper increase in the Vickers hardness. Both sets of measurement results show a consistent upward trend, confirming that the solid solution strengthening and grain refinement effects caused by the dissolution of element V can enhance the material's mechanical properties [17].

Through comprehensive analysis of the mechanical properties of the $Cr_2(Ti_{1-x}V_x)AlC_2$ (x = 0–0.5) series samples, it is evident that V solute inclusion contributes to the overall enhancement of both strength and toughness in the material. Based on the Vickers hardness indentation morphology (Fig. 8), it can be clearly observed that as the V content increases, the warped fracture zone around the indentation gradually diminishes. This morphological feature is fully consistent with the progressively enhanced K_{IC} calculated via the energy-based approach (Fig. 9(a)) [28]. The fracture toughness of the V0.5 sample reached its maximum value (6.39±0.20 MPa·m$^{1/2}$), representing an approximately 5.1% increase compared to the V0 sample (6.08±0.19 MPa·m$^{1/2}$). This indicates that the solid solution of V improves the macroscopic toughness of the material [69].

Simultaneously, the E^2/H (capacity of energy dissipation) and H^3/E^2 (resistance to plastic deformation) of the samples were calculated based on the elastic modulus and nanoindentation

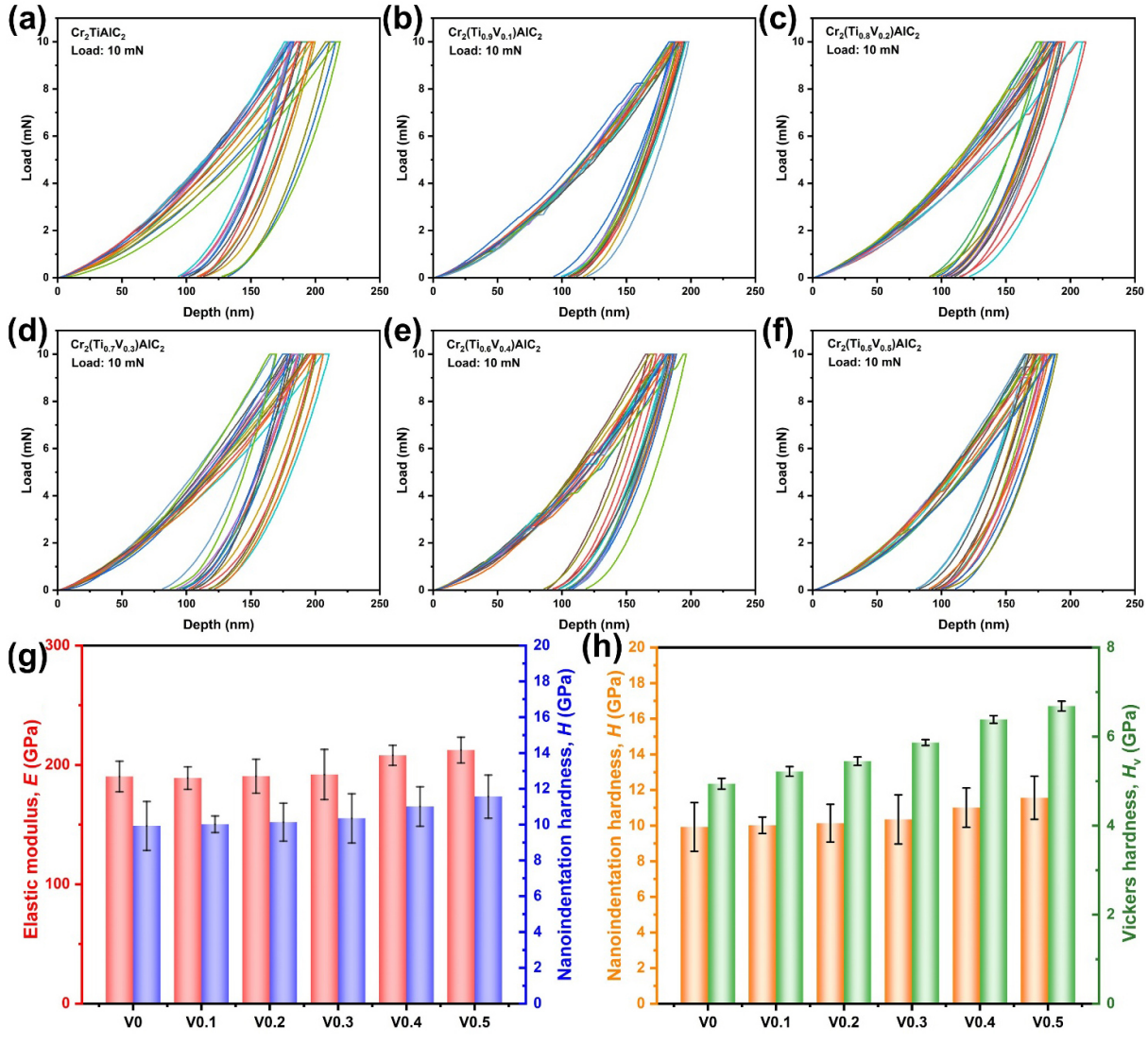


Fig. 7 Load-displacement curves of $Cr_2(Ti_{1-x}V_x)AlC_2$ (x = 0–0.5) MAXs via nanoindentation with a peak load of 10 mN: (a) V0, (b) V0.1, (c) V0.2, (d) V0.3, (e) V0.4, and (f) V0.5. (g) Nanoindentation hardness and elastic modulus of six MAXs. (h) Nanoindentation hardness and Vickers hardness of six MAXs.

Table 5 Performance comparison of $Cr_2(Ti_{1-x}V_x)AlC_2$ (x = 0–0.5) series samples

Sample	E (GPa)	H (GPa)	H_v (GPa)	K_{IC} (MPa·m$^{1/2}$)	E^2/H (GPa)	H^3/E^2 (GPa)
V0	190.31±12.86	9.93±1.37	4.94±0.12	6.08±0.19	3649.00	0.0270
V0.1	188.99±9.44	10.02±0.46	5.22±0.11	6.10±0.41	3564.98	0.0282
V0.2	190.54±14.22	10.14±1.06	5.45±0.96	6.16±0.24	3581.51	0.0287
V0.3	191.97±21.03	10.35±1.38	5.87±0.67	6.25±0.22	3561.29	0.0301
V0.4	208.02±8.38	11.01±1.10	6.39±0.85	6.35±0.61	3928.82	0.0309
V0.5	212.48±10.78	11.56±1.21	6.68±0.11	6.39±0.20	3904.02	0.0343

hardness (Fig. 9(b)) [68]. E^2/H and H^3/E^2 are positively correlated with K_{IC}. First, E^2/H reflects a material's ability to store elastic energy prior to yielding, which is directly related to its resistance to crack initiation [68]. At the same time, a higher H^3/E^2 reduces the size of the plastic zone around the crack tip and lowers the residual tensile stress, thereby inhibiting crack propagation [70]. The E^2/H value fluctuated slightly at lower V content levels (Table 5). When the V addition ratio increased to 0.4 and 0.5, the values significantly improved to 3928.82 and 3904.02 GPa, respectively, markedly higher than the V0 sample (3649.00 GPa).

The abrupt increase in E^2/H at x = 0.4 and 0.5 is attributed to two synergistic effects near the solubility limit. First, as the V content approaches x = 0.5, the ordered occupation of V at the 2a sites reaches saturation, maximizing local lattice distortion and enhancing dislocation slip resistance, resulting in a cumulative solid-solution strengthening effect that intensifies nonlinearly [32]. Simultaneously, as the V content increases, the higher-stiffness V–C bonds gradually replace the Ti–C bonds, leading to a step-like increase in the elastic modulus E (an increase of approximately 11.6% from V0 to V0.5) [71]. The combined effect of the enhanced dislocation resistance and the rise in the elastic modulus E results in a nonlinear jump in E^2/H. This demonstrates that incorporating V endows the material with enhanced crack initiation resistance. Additionally, H^3/E^2 monotonically increases

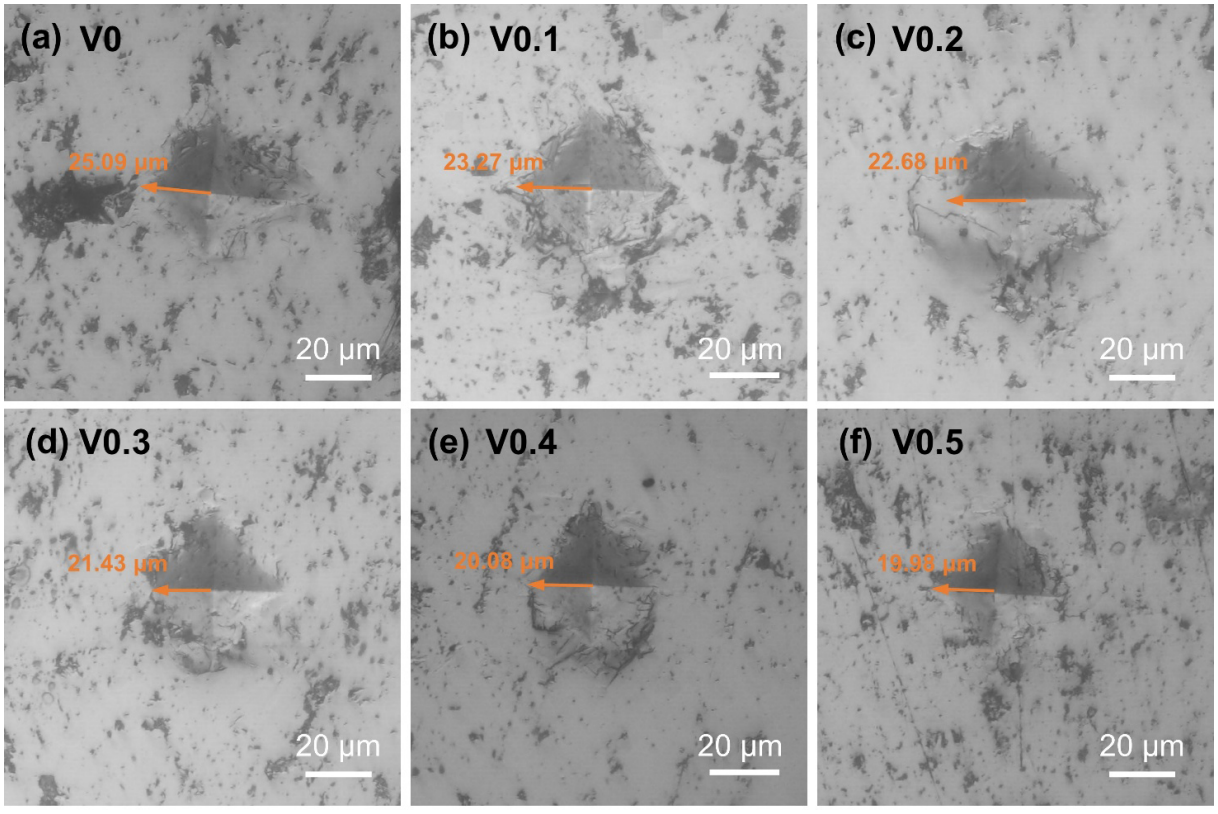


Fig. 8 Vickers hardness indentation microstructure of $Cr_2(Ti_{1-x}V_x)AlC_2$ (x = 0–0.5) samples: (a) V0, (b) V0.1, (c) V0.2, (d) V0.3, (e) V0.4, and (f) V0.5.

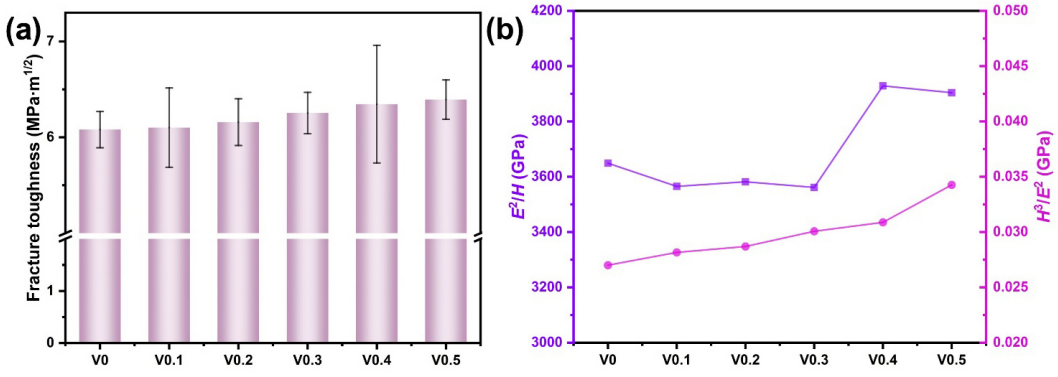


Fig. 9 (a) Fracture toughness diagram of $Cr_2(Ti_{1-x}V_x)AlC_2$ (x = 0–0.5) samples. (b) E^2/H and H^3/E^2 values of the samples.

with increasing V content (Table 5), with the V0.5 sample reaching the maximum value (0.0343 GPa). Compared to the V0 sample (0.0270 GPa), this represents an approximate 27.0% improvement, indicating that the out-of-plane chemically ordered V incorporation synergistically enhances the material's resistance to permanent deformation while simultaneously increasing its hardness [28]. While existing research remains controversial regarding whether E^2/H and H^3/E^2 can serve as universal surrogate indicators of toughness [72], in this study, the V0.5 specimens simultaneously exhibited the highest K_{IC} (5.1% increase), E^2/H (7.0% increase), and H^3/E^2 (27.0% increase). Meanwhile, the trends in these parameters were consistent across the series of specimens, confirming a positive synergy among the three and providing a basis for using E^2/H and H^3/E^2 as reasonable supplementary indicators for toughness evaluation.

4 Conclusions

A series of $Cr_2(Ti_{1-x}V_x)AlC_2$ (x = 0–0.6) quinary o-MAX materials was synthesized, and their phase composition, crystal structure, and chemical ordering were analyzed. Subsequently, nanoindentation and Vickers hardness tests were conducted, with fracture toughness evaluated using the indentation method. Analysis of the material's structure and properties elucidated the influence of chemical composition on material performance, yielding the following conclusions:

(1) Through XRD Rietveld refinement and HAADF-STEM/EDS analysis, the solid solution of V in Cr_2TiAlC_2 can preserve the out-of-plane chemical ordering at a maximum V content of x = 0.5, in which Cr atoms occupy the 4*f* Wyckoff sites, while V selectively forms solid solutions with Ti at the 2*a* Wyckoff sites. When the V content exceeds the solid solution limit (e.g., x = 0.6), V and Ti migrate to the 4*f* site, causing an ordered–disordered transition in the lattice.

(2) The out-of-plane chemically ordered incorporation of V achieves comprehensive enhancement of material mechanical properties. Compared to the V0 sample, the optimal composition V0.5 sample exhibits a 16.4% increase in nanoindentation

hardness (11.56±1.21 GPa), a 35.2% enhancement in Vickers hardness (6.68±0.11 GPa), and an approximately 5.1% improvement in fracture toughness (6.39 MPa·$m^{1/2}$). Additionally, the H^3/E^2 ratio increases by approximately 27.0%, indicating a significant enhancement in the material's resistance to plastic deformation and achieving a synergistic effect of strengthening and toughening.

(3) The substitution of Ti with V, which has a smaller atomic radius, induces continuous lattice contraction (approximately 0.62% contraction along the *a*-axis and 0.47% contraction along the *c*-axis), confirming the formation of a solid solution. In addition, as the vanadium content increased, the average grain size decreased from 9.11 μm (V0 sample) to 6.33 μm (V0.5 sample). The grain refinement effect, which combines lattice contraction and selective element occupation, constitutes the microstructural mechanism underlying both solid solution strengthening and grain refinement strengthening. Simultaneously, the E^2/H ratio of the V0.5 sample significantly increases, reflecting enhanced energy dissipation capacity and crack initiation resistance, ultimately manifesting as superior mechanical properties. This work not only expands the variety of o-MAX materials but also provides a clear strategy for tailoring the properties of such materials by selecting site-specific solid solution elements.

Acknowledgements

The authors are grateful for the financial support from the National Natural Science Foundation of China (Nos. 52275212 and 52572085), the fund of the State Key Laboratory of Solidification Processing in NPU (No. 2025-TS-09), the "Special Lubrication and Sealing for Aerospace" Shaanxi Provincial Science and Technology Innovation Team (No. 2024RSCXTD-63), and the research fund from the Analytical & Testing Center of Northwestern Polytechnical University (No. 2023T012). In addition, the authors would like to thank Dr. Xiubo Yang and Dr. Ying Ding at the Analytic & Testing Center of NPU for assistance with atomic-resolution TEM characterization.

Author contributions

Cheng-Feng Du: Conceptualization, formal analysis, writing – review & editing, and funding acquisition. Linze Fan: Data curation, formal analysis, investigation, and writing – original draft. Xuan Luo: Investigation, methodology. Yaqing Xue: Investigation, methodology. Shiyao Lei: Methodology, resources. Yifei Xiao: Methodology. Wenbo Wu: Resources. Weihong Qi: Resources, software. Hong Yu: Writing – review & editing, supervision, and funding acquisition.

Availability of data and materials

The data that support the findings of this study are available from the corresponding author upon reasonable request.

Competing interests

The authors have no competing interests to declare that are relevant to the content of this article.

Electronic Supplementary Material

Supplementary material is available in the online version of this article at https://doi.org/10.26599/JAC.2026.9221336.

References

[1] Anasori B, Lukatskaya MR, Gogotsi Y. 2D metal carbides and nitrides (MXenes) for energy storage. *Nat Rev Mater* 2017, **2**: 16098.

[2] Snyder RM, Juelsholt M, Kalha C, *et al.* Detailed analysis of the synthesis and structure of MAX phase $(Mo_{0.75}V_{0.25})_5AlC_4$ and its MXene sibling $(Mo_{0.75}V_{0.25})_5C_4$. *ACS Nano* 2023, **17**: 12693–12705.

[3] Wyatt BC, Thakur A, Nykiel K, *et al.* Design of atomic ordering in $Mo_2Nb_2C_3T_x$ MXenes for hydrogen evolution electrocatalysis. *Nano Lett* 2023, **23**: 931–938.

[4] Chang YK, Zhao HL, Liu X, *et al.* Etching-time-regulated strategy toward delaminated Mo_2CT_x MXene for tailoring electromagnetic wave absorption. *J Adv Ceram* 2024, **13**: 1795–1806.

[5] Sokol M, Natu V, Kota S, *et al.* On the chemical diversity of the MAX phases. *Trends Chem* 2019, **1**: 210–223.

[6] Barsoum MW. The $M_{N+1}AX_N$ phases: A new class of solids: Thermodynamically stable nanolaminates. *Prog Solid State Ch* 2000, **28**: 201–281.

[7] Yu H, Xue LL, Xue YQ, *et al.* Mapping the structure and chemical composition of MAX phase ceramics for their high-temperature tribological behaviors. *Carbon Energy* 2024, **6**: 597.

[8] Barsoum MW, Radovic M. Elastic and mechanical properties of the MAX phases. *Ann Rev Mater Res* 2011, **41**: 195–227.

[9] Radovic M, Barsoum MW. MAX phases: Bridging the gap between metals and ceramics. *Am Ceram Soc Bull* 2013, **92**: 20–27.

[10] Dahlqvist M, Barsoum MW, Rosen J. MAX phases—Past, present, and future. *Mater Today* 2024, **72**: 1–24.

[11] Wen B, Liu YJ, Cao L, *et al.* Synthesis of two new o-MAX phases Mo_2VAlC_2 and $Mo_2V_2AlC_3$ and their derivatives o-MXene $Mo_2VC_2T_x$ and $Mo_2V_2C_3T_x$. *J Eur Ceram Soc* 2025, **45**: 116964.

[12] Li HB, Su YF, Hu TC, *et al.* Research progress on ternary layered MAB phases ceramics and their mechanical and tribological properties. *Tribology* 2025, **45**: 1084–1100.

[13] Tian ZH, Hu FY, Zhang PG, *et al.* High-entropy engineering of A-site in MAX phases toward superior microwave absorption properties. *Matter* 2025, **8**: 102367.

[14] Dahlqvist M, Lu J, Meshkian R, *et al.* Prediction and synthesis of a family of atomic laminate phases with Kagomé-like and in-plane chemical ordering. *Sci Adv* 2017, **3**: 1700642.

[15] Jin KJ, Hu Z, Tan H, *et al.* Tribological properties and shock resistances of aluminum bronze–Ti_3AlC_2 composites. *Tribology* 2025, **45**: 35–45. (in Chinese)

[16] Li Y, Ma K, Xu JJ, *et al.* Mechanism of Cr_2AlC as a diffusion barrier to retard degradation of NiCrAlY coatings on Ti65 alloy. *Corros Commun* 2025, **20**: 190–200.

[17] Zhou SH, Yuan JH, Wu HC, *et al.* Size-dependent uniform deformation transitions enabling hardness and toughness enhancement of nanocrystalline Cr_2AlC MAX phase. *J Mater Sci Technol* 2025, **232**: 170–180.

[18] Dahlqvist M, Rosen J. Predictive theoretical screening of phase stability for chemical order and disorder in quaternary 312 and 413 MAX phases. *Nanoscale* 2020, **12**: 785–794.

[19] Dahlqvist M, Rosen J. Order and disorder in quaternary atomic laminates from first-principles calculations. *Phys Chem Chem Phys* 2015, **17**: 31810–31821.

[20] Chen HX, Zhang ZL, Wen XC, *et al.* Discovery of Ge-based o-MAX phases with robust out-of-plane Ti–Cr chemical ordering. *J Mater Sci Technol* 2026, **267**: 84–92.

[21] Liu ZM, Zheng LY, Sun LC, *et al.* $(Cr_{2/3}Ti_{1/3})_3AlC_2$ and $(Cr_{5/8}Ti_{3/8})_4AlC_3$: New MAX-phase compounds in Ti–Cr–Al–C system. *J Am Ceram Soc* 2014, **97**: 67–69.

[22] Xue YQ, Wang CC, Zeng QY, *et al.* Ordered metal substitution in Ti_3AlC_2 and the effect on tribological behaviors in a wide temperature range. *Tribol Int* 2023, **178**: 108009.

[23] Liu ZM, Yang J, Qian YH, *et al.* *In-situ* reaction synthesis and mechanical properties of quaternary MAX phase $(Cr_{2/3}Ti_{1/3})_3AlC_2$. *Ceram Int* 2020, **46**: 22854–22860.

[24] Liu ZM, Yang J, Qian YH, *et al.* High temperature oxidation behavior of quaternary ordered $(Cr_{2/3}Ti_{1/3})_3AlC_2$-based MAX ceramic. *Corros Sci* 2021, **183**: 109317.

[25] Feng XH, Li N, Chen BY, *et al.* Thermodynamics for the non-conventional synthesizing of out-of-plane ordered double-transition metal "312" and "413" MAX phases (o-MAX): A high throughput

linear programing first-principles calculation. *J Mater Sci Technol* 2023, **134**: 81–88.
[26] Wang KH, Zhang Y, Ma GS, *et al.* Exceptional mechanical properties of $(Ti_{1-x}Zr_x)_2AlC$ MAX phase coatings with amorphous–nanocrystalline oxidation layers. *J Adv Ceram* 2026, **15**: 9221201.
[27] Ma GS, Zhang AF, Wang ZY, *et al.* MAX phase coatings: Synthesis, protective performance, and functional characteristics. *Mater Horiz* 2025, **12**: 1689–1710.
[28] Zhang Y, Zhang SW, Zhang AF, *et al.* Breaking the trade-off of hardness–ductility in $(Cr_{1-x}Mo_x)_2AlC$ MAX phase coatings via a hierarchical structure. *J Adv Ceram* 2024, **13**: 1748–1758.
[29] Du CF, Wang CC, Xu MF, *et al.* Miscible chemical ordering in Ti–Cr–Mo quinary system by solid solution of $Mo_2Ti_2AlC_3$ and $Cr_{2.5}Ti_{1.5}AlC_3$ o-MAXs. *Nat Commun* 2025, **16**: 3011.
[30] Du CF, Xue YQ, Zeng QY, *et al.* Mo-doped Cr–Ti–Mo ternary o-MAX with ultra-low wear at elevated temperatures. *J Eur Ceram Soc* 2022, **42**: 7403–7413.
[31] Xue YQ, Wang CC, Lei SY, *et al.* Synthesis of quinary M_3AlC_2 (M = Ti, Cr, and Mo) *o*-MAX and its energy dissipation-enhanced anti-wear performance. *Tribol Int* 2026, **213**: 111018.
[32] Xue YQ, Yu H, Liang HW, *et al.* Transformation of chemical ordering and configuration entropy in quaternary $Cr_xTi_{0.75}Mo_{0.75}V_{1.5-x}AlC_2$ MAX system. *J Adv Ceram* 2024, **13**: 1861–1871.
[33] Wyatt BC, Yang YN, Michałowski PP, *et al.* Order-to-disorder transition due to entropy in layered and 2D carbides. *Science* 2025, **389**: 1054–1058.
[34] Xue YQ, Yu H, Liang HW, *et al.* Optimizing the Cr and V content in quaternary MAX phase for high-temperature lubricity and wear resistance. *Tribol Int* 2025, **204**: 110525.
[35] Yuan R, Zhang YP, Wang ZY, *et al.* Tribological property of V_2AlC MAX phase coating over wide temperature range. *Tribology* 2023, **43**: 537–548. (in Chinese)
[36] Liu L, Zhang MT, Zhuang QF, *et al.* Mechanism-driven strengthening of MAX phase ceramics by $Ti_3C_2T_x$ MXene: A comparative study on Cr_2AlC and Ta_2AlC. *J Adv Ceram* 2025, **14**: 9221134.
[37] Caspi EN, Chartier P, Porcher F, *et al.* Ordering of (Cr,V) layers in nanolamellar $(Cr_{0.5}V_{0.5})_{n+1}AlC_n$ compounds. *Mater Res Lett* 2015, **3**: 100–106.
[38] Du CF, Wang CC, Liang HW, *et al. In-situ* liquid lubrication with bearing effect on a semi-out-of-plane ordered ternary $(TiVCr)_3AlC_2$ MAX at 800 °C. *J Eur Ceram Soc* 2023, **43**: 7341–7353.
[39] Xu M, Geng JH, Liu JX, *et al.* Enhancement of X-ray detection efficiency by nanoparticles in organic semiconductor film. *J Mater Sci Technol* 2026, **253**: 280–288.
[40] Toby BH, Von Dreele RB. *GSAS-II*: The genesis of a modern open-source all purpose crystallography software package. *J Appl Crystallogr* 2013, **46**: 544–549.
[41] Wang L, Geng YS, Tieu AK, *et al. In-situ* formed graphene providing lubricity for the FeCoCrNiAl based composite containing graphite nanoplate. *Compos Part B—Eng* 2021, **221**: 109032.
[42] Hempel JL, Meyer A, Hill R, *et al.* Validating a facile approach to measuring fracture toughness by instrumented indentation without imaging crack-lengths. *MRS Commun* 2022, **12**: 279–282.
[43] Cheng YT, Li ZY, Cheng CM. Scaling relationships for indentation measurements. *Philos Mag A* 2002, **82**: 1821–1829.
[44] Pharr GM. Measurement of mechanical properties by ultra-low load indentation. *Mat Sci Eng A—Struct* 1998, **253**: 151–159.
[45] Vanderbilt D. Soft self-consistent pseudopotentials in a generalized eigenvalue formalism. *Phys Rev B* 1990, **41**: 7892–7895.
[46] Perdew JP, Wang Y. Pair-distribution function and its coupling-constant average for the spin-polarized electron gas. *Phys Rev B* 1992, **46**: 12947–12954.
[47] Clark SJ, Segall MD, Pickard CJ, *et al.* First principles methods using CASTEP. *Z Krist—Cryst Mater* 2005, **220**: 567–570.
[48] Zunger A, Wei SH, Ferreira LG, *et al.* Special quasirandom structures. *Phys Rev Lett* 1990, **65**: 353–356.
[49] Dahlqvist M, Alling B, Rosén J. Stability trends of MAX phases from first principles. *Phys Rev B* 2010, **81**: 220102.
[50] Ji J, Zhan XY, Jiang XM, *et al.* Synthesis and DFT calculations of high entropy six-component Ti-based MAX of $(Ti,M)_2AlC$ (M = Zr, Nb, Ta, Mo, W). *Vacuum* 2025, **239**: 114332.
[51] Meng CH, Xu MF, Lei SY, *et al.* Synthesis, chemical bonding, and mechanical properties of Ti–Nb–Hf ternary solid solution MAXs. *J Mater Chem A* 2025, **13**: 31632–31641.
[52] Cao L, Zhang QQ, Du LJ, *et al.* Synthesis and characterization of high entropy $(TiVNbTaM)_2AlC$ (M = Zr, Hf) ceramics. *J Adv Ceram* 2024, **13**: 237–246.
[53] Xu KX, Zhou SH, Wang ZY, *et al.* Prism-plane-textured Cr_2AlC MAX-phase coatings with superior resistance to coupled thermal–salt–steam corrosion. *Corros Sci* 2026, **258**: 113395.
[54] Du CF, Zeng QY, Wang YF, *et al.* Synergism of Al and Si occurs on corrosion of $Ti_3Al_{1-x}Si_xC_2$ MAX in the static Pb–Bi eutectic at 550 °C. *Corros Sci* 2024, **233**: 112068.
[55] Qin F, Fan TX, Zhang D. Thermodynamic effects of alloying elements on solid-state interfacial reactions in a multicomponent system: Theoretical treatment and application in SiC_f/Ti composites. *Metall Mater Trans A* 2009, **40**: 462–471.
[56] Li ZC, Wang ZY, Ma GS, *et al.* High-performance Cr_2AlC MAX phase coatings for ATF application: Interface design and oxidation mechanism. *Corros Commun* 2024, **13**: 27–36.
[57] Zhao S, Xiao H, Li YX, *et al.* Multi-stage phase transformation pathways in MAX phases. *Nat Commun* 2025, **16**: 1554.
[58] Hu J, Feng Y, Zhao H, *et al.* Ti_3SiC_2 irradiation damage at electron beam energy levels of 120 keV and 200 keV. *Mater Lett* 2021, **285**: 129064.
[59] Du CF, Xue YQ, Liang HW, *et al.* Exploring the oxidation behaviors of the Ti–V–Cr–Mo high-entropy MAX at 800 °C for its self-lubricity. *J Mater Sci Technol* 2024, **187**: 49–62.
[60] Murphy ST, Chroneos A, Jiang C, *et al.* Deviations from Vegard's law in ternary III–V alloys. *Phys Rev B* 2010, **82**: 073201.
[61] Halim J, Chartier P, Basyuk T, *et al.* Structure and thermal expansion of $(Cr_xV_{1-x})_{n+1}AlC_n$ phases measured by X-ray diffraction. *J Eur Ceram Soc* 2017, **37**: 15–21.
[62] Zapata-Solvas E, Hadi MA, Horlait D, *et al.* Synthesis and physical properties of $(Zr_{1-x},Ti_x)_3AlC_2$ MAX phases. *J Am Ceram Soc* 2017, **100**: 3393–3401.
[63] Li HB, Fan HZ, Su YF, *et al.* Quaternary layered boride Ti_4MoSiB_2: A structure–function integrated high-temperature self-lubricating and negative-wear material. *Adv Mater* 2025, **37**: 2418995.
[64] Tian ZH, Zhang PG, Sun WW, *et al.* Vegard's law deviating $Ti_2(Sn_xAl_{1-x})C$ solid solution with enhanced properties. *J Adv Ceram* 2023, **12**: 1655–1669.
[65] Tunca B, Lapauw T, Karakulina OM, *et al.* Synthesis of MAX phases in the Zr–Ti–Al–C system. *Inorg Chem* 2017, **56**: 3489–3498.
[66] Liu ZM, Wu ED, Wang JM, *et al.* Crystal structure and formation mechanism of $(Cr_{2/3}Ti_{1/3})_3AlC_2$ MAX phase. *Acta Mater* 2014, **73**: 186–193.
[67] Dippo OF, Vecchio KS. A universal configurational entropy metric for high-entropy materials. *Scripta Mater* 2021, **201**: 113974.
[68] Lei SY, Meng CH, Fan LZ, *et al.* Synthesis of Ti–Nb–Hf quinary M_2AlC MAX ceramics and the effects of Hf incorporation on the anti-wear performance up to 800 °C. *Ceram Int* 2025, **51**: 52849–52863.
[69] Guo YN, Staedler T, Müller J, *et al.* A detailed analysis of the determination of fracture toughness by nanoindentation induced radial cracks. *J Eur Ceram Soc* 2020, **40**: 276–289.
[70] Beake BD. The influence of the H/E ratio on wear resistance of coating systems—Insights from small-scale testing. *Surf Coat Tech* 2022, **442**: 128272.
[71] Bai YL, He XD, Wang RG, *et al.* An *ab initio* study on compressibility of Al-containing MAX-phase carbides. *J Appl Phys* 2013, **114**: 173709.
[72] Chen XJ, Du Y, Chung YW. Commentary on using H/E and H^3/E^2 as proxies for fracture toughness of hard coatings. *Thin Solid Films* 2019, **688**: 137265.